

Simulation of eccentricity effects on short- and long-normal logging measurements using a Fourier-*hp*-finite-element method*

Myung Jin Nam^{1,4} David Pardo^{2,4} Carlos Torres-Verdín³ Seho Hwang^{1,5}
Kwon Gyu Park¹ Changhyun Lee¹

¹Korea Institute of Geoscience and Mineral Resources (KIGAM), Gwahang-no 92, Yuseong-gu, Daejeon 305-350, Korea.

²IKERBASQUE, Basque Foundation for Science and BCAM – Basque Centre for Applied Mathematics, Bizkaia Technology Park, Building 500, 48160 Derio, Spain.

³Department of Petroleum and Geosystems Engineering, The University of Texas, Austin, TX 78712-1080, USA.

⁴Formerly with Department of Petroleum and Geosystems Engineering, The University of Texas, Austin, TX 78712-1080, USA.

⁵Corresponding author. Email: hwangse@kigam.re.kr

Abstract. Resistivity logging instruments are designed to measure the electrical resistivity of a formation, and this can be directly interpreted to provide a water-saturation profile. However, resistivity logs are sensitive to borehole and shoulder-bed effects, which often result in misinterpretation of the results. These effects are emphasised more in the presence of tool eccentricity. For precise interpretation of short- and long-normal logging measurements in the presence of tool eccentricity, we simulate and analyse eccentricity effects by combining the use of a Fourier series expansion in a new system of coordinates with a 2D goal-oriented high-order self-adaptive *hp* finite-element refinement strategy, where *h* denotes the element size and *p* the polynomial order of approximation within each element. The algorithm automatically performs local mesh refinement to construct an optimal grid for the problem under consideration. In addition, the proper combination of *h* and *p* refinements produces highly accurate simulations even in the presence of high electrical resistivity contrasts. Numerical results demonstrate that our algorithm provides highly accurate and reliable simulation results. Eccentricity effects are more noticeable when the borehole is large or resistive, or when the formation is highly conductive.

Key words: eccentricity, finite-element method, *hp*, normal logging, self-adaptivity.

Introduction

Borehole resistivity logging can be used to directly determine water-saturation profiles because the electrical conductivity of rocks depends on pore volume, pore connectivity, and electrical conductivity of pore fluid. Since the development of borehole electrical methods by Doll (1951, 1953), Schlumberger Well Surveying Corporation (SWSC) (Anon., 1949, 1969), and Pirson (1963), resistivity logging measurements have been extensively conducted for hydrocarbon reservoir characterisation and surveillance. Even though resistivity logging devices have been mainly developed for the oil industry, these tools have been also widely used in ground water and engineering geophysical problems. Nowadays, borehole resistivity measurements aim to be applied for monitoring injected CO₂ in a CO₂ sequestration site, which is a worldwide matter of primary concern due to global warming. The main limitations of resistivity logging are due to large-borehole effects and shoulder-bed effects on the measurements.

Forward numerical modelling of resistivity logging measurements is important for resistivity well logging data interpretation since modelling techniques are used to understand the main characteristics of logging devices. Electrical resistivity logs have been simulated using differential equation methods

(e.g. Hakvoort et al., 1998; Tamarchenko et al., 1999), integral equation methods (e.g. Howard and Chew, 1992), hybrid methods (e.g. Tsang et al., 1984; Tamarchenko and Druskin, 1993), or neural networks approaches (e.g. Zhang et al., 2002). These methods generate synthetic log responses for a given resistivity earth model that often can be used to analyse borehole effects or shoulder-bed effects.

The borehole effects and shoulder-bed effects are known to be more profound when the tool is decentralised. If the logging tool is eccentric from the axis of the borehole, the resulting geometry needs to be analysed in three spatial dimensions. When we do not consider the actual logging instrument, a Dirac delta source can be used for the simulation of resistivity logging measurements. For the Dirac delta source, it is possible to make a Fourier series expansion in one spatial dimension and solve the resulting sequence of 2D problems (one problem for each Fourier mode), which are independent of each other, and thus, can be independently solved by using a 2D simulator. This method using Fourier expansion reduces the problem to a 2.5D one (Tabarovsky et al., 1996). A 2.5D problem is the one that can be solved as a sequence of 2D problems. From the computational point of view, a 2.5D problem is more expensive than a 2D problem, but cheaper

*Part of this paper was presented at the 9th SEGJ International Symposium (2009).

than a 3D problem, which explains why it is referred to as 2.5D. However, the applicability of the 2.5D method is limited since the actual logging instrument cannot be simulated.

In this paper, we simulate short- and long-normal resistivity logging measurements in the presence of tool eccentricity. In our simulations, we consider a logging tool with realistic tool properties and dimensions, and thus the resulting 3D geometry cannot be solved with a 2.5D method. The complexity of arbitrary 3D geometries increases the computational requirements. We reduce the computational complexity of 3D algorithms by employing a particular system of coordinates which separates the decentralised tool from the borehole. The idea of mapping the 3D geometry into a particular system of coordinates for these purposes was briefly introduced in Pardo et al. (2008).

We construct a new system of coordinates $\zeta = (\zeta_1, \zeta_2, \zeta_3)$ for which material properties are invariant with respect to the quasi-azimuthal direction ζ_2 . Since any function in the new system of coordinates is also periodic, it can therefore be expressed in terms of its Fourier series expansion with respect to ζ_2 . Using a Fourier series expansion in the new system of coordinates, we can derive the corresponding 3D formulation consisting of a sequence of 2D problems, in which each 2D problem couples in a weak sense with the remaining 2D problems. Thanks to the weak coupling between Fourier modes, we can obtain a converged solution with a low computational cost. This is the main advantage of our 3D formulation over traditional formulations.

To solve the resulting coupled 2D problems in our 3D formulation, we employ a goal-oriented, self-adaptive hp finite-element (FE) method (Pardo et al., 2006b), where h denotes the element size and p the polynomial order of approximation within each element. The algorithm automatically conducts local mesh refinements to construct an optimal grid (with exponential convergence) for the problem under consideration. In addition, the proper combination of h and p refinements produces highly accurate simulations even in the presence of high contrast of material properties. Numerical results indicate that our 3D algorithm produces accurate simulation of long- and short-normal logging measurements in the presence of tool eccentricity with a small number of Fourier modes and a limited computational cost.

Normal logging instrument

For the simulation of long- and short-normal logging measurements, we implement a specific commercial tool configuration (Figure 1), which has been used in the Korea Institute of Geoscience and Mineral Resources (KIGAM) for several years. Each electrode in the simulation has been placed at the same location with the same vertical dimension as that of the commercial tool. Potential electrodes for long- and short-normal logging are located 64 inches above and 16 inches below the current electrode, respectively (Figure 1). We assume that the resistivity of all the electrodes is equal to $10^{-6} \Omega \cdot \text{m}$, while the resistivity of the mandrel is $10^6 \Omega \cdot \text{m}$, resulting in a resistivity contrast at the interfaces between electrodes and insulator equal to 10^{12} .

Simulation method

Variational formulation in the Cartesian system of coordinates

Resistivity applications for normal logging devices are based on the direct current (DC) assumption, and thus are governed by the

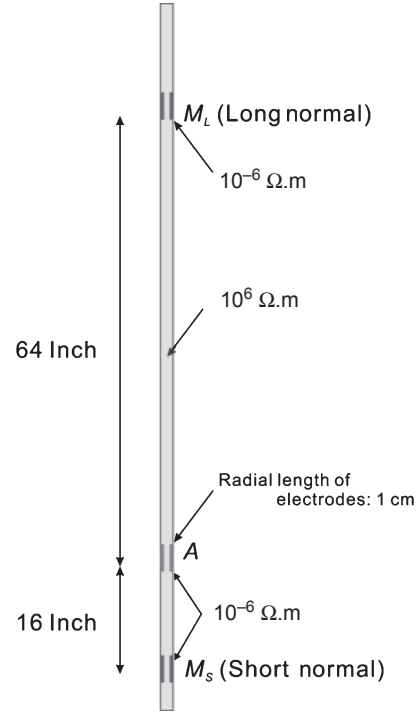


Fig. 1. Configuration of a commercial normal logging tool with one current electrode A , and two potential electrodes, M_L and M_S , for long- and short-normal measurements, respectively.

electrostatic equation in a (simply connected) spatial domain Ω , given by

$$\nabla \cdot (\sigma \nabla u) = \nabla \cdot \mathbf{j}^{\text{imp}}, \quad (1)$$

where σ is the conductivity, \mathbf{j}^{imp} is the impressed electric current density measured in A/m^2 and u is the electrostatic potential measured in volts. In the case of simply connected domains, the electric field is given by $\mathbf{E} = -\nabla u$. On the boundary of the domain far from the electrode, denoted by Γ_D , where the electric potential is approximately zero, a homogeneous Dirichlet boundary condition is assigned for simplicity, i.e. $u|_{\Gamma_D} = 0$.

Multiplication of equation 1 by a test function

$$v \in H_D^1(\Omega) = \{u \in L^2(\Omega) : u|_{\Gamma_D} = 0, \quad \nabla u \in L^2(\Omega)\},$$

(where $H_D^1(\Omega)$ is the space of admissible solutions, and L^2 (and L^2) are the spaces of scalar (and vector, respectively) functions whose square is integrable) and integration of the resulting equation by parts over Ω , delivers a variational formulation for the electrostatic equation

$$\begin{cases} \text{Find } u \in H_D^1(\Omega) \text{ such that:} \\ \int_{\Omega} \sigma \nabla u \cdot \nabla v \, dV = \int_{\Omega} \nabla \cdot \mathbf{j}^{\text{imp}} v \, dV + \int_{\Gamma_N} g v \, dS, \quad \forall v \in H_D^1(\Omega), \end{cases} \quad (2)$$

where $g = (\sigma \nabla u) \cdot \mathbf{n}$ is a prescribed flux defined on Γ_N , and \mathbf{n} is the unit normal outward (with respect to Ω) vector.

New system of coordinates for measurements with tool eccentricity in vertical boreholes

For logging measurements with tool eccentricity (Figure 2a), we employ a new system of coordinates $\zeta = (\zeta_1, \zeta_2, \zeta_3)$ (Figure 2; Pardo et al., 2008) defined in terms of a Cartesian system of

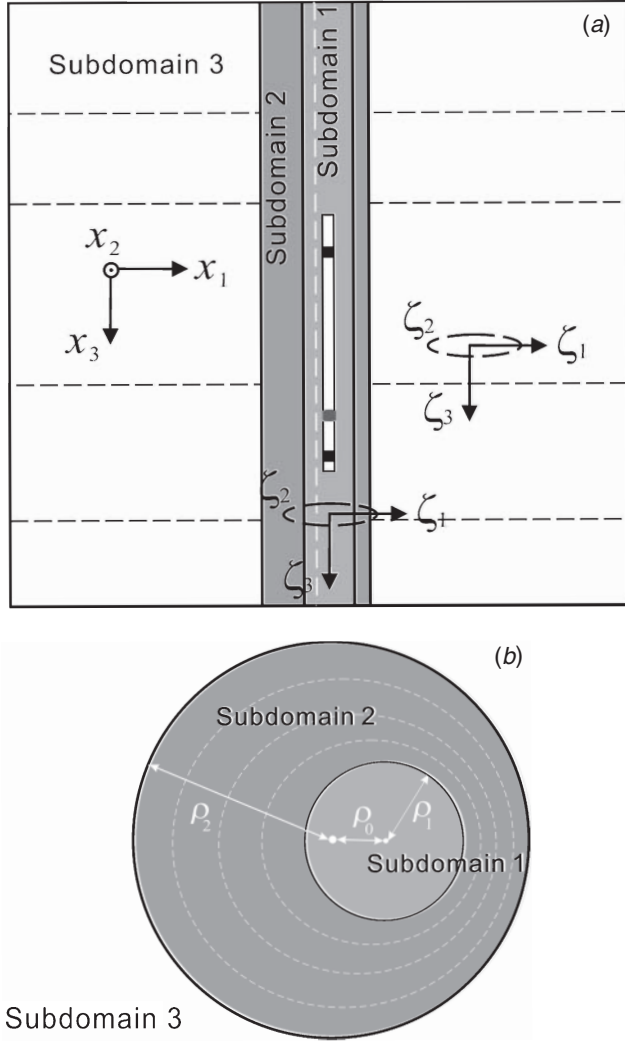


Fig. 2. (a) Cross-section of a well with an eccentric tool, corresponding to $\zeta_2 = 0$ in a new system of coordinates. Both x_3 -direction (in a Cartesian system of coordinates) and ζ_3 -direction (in a new system of coordinates) correspond to the axis of the borehole with ζ_3 positive downward along the axis of the borehole. The new system of coordinates employs three domains having different systems of coordinates. As described in both the cross section panel (a) and the plan view panel (b), subdomain 1 is a part of the borehole that includes the logging instrument, while subdomain 3 corresponds to the formation. Subdomain 2 is the part of the borehole not contained in subdomain 1, and glues subdomain 1 with subdomain 3 so that the resulting non-orthogonal system of coordinates is globally continuous, bijective, and with a positive Jacobian. The origin of both systems lies on the axis of the borehole.

coordinates $\mathbf{x} = (x_1, x_2, x_3)$ (with x_3 positive downward along the axis of the borehole) as

$$\begin{cases} x_1 = f_1(\zeta_1) + \zeta_1 \cos \zeta_2 \\ x_2 = \zeta_1 \sin \zeta_2 \\ x_3 = \zeta_3 \end{cases}, \quad (3)$$

where f_1 is defined for given ρ_1 and ρ_2 as

$$f_1(\zeta_1) = \begin{cases} \rho_0 & \zeta_1 < \rho_1 \\ \rho_0(\zeta_1 - \rho_2)/(\rho_1 - \rho_2) & \rho_1 \leq \zeta_1 \leq \rho_2 \\ 0 & \zeta_1 > \rho_2 \end{cases}, \quad (4)$$

with the corresponding derivative expressed as

$$f_1'(\zeta_1) = f_1' = \begin{cases} 0, & \zeta_1 < \rho_1 \\ \frac{-\rho_0}{\rho_2 - \rho_1}, & \rho_1 \leq \zeta_1 \leq \rho_2 \\ 0, & \zeta_1 > \rho_2 \end{cases}, \quad (5)$$

where the surface $\zeta_1 = \rho_1$ is the interface between subdomains 1 and 2, and the surface $\zeta_1 = \rho_2$ is the interface between subdomains 2 and 3, as shown in Figure 2. Note that the new system of coordinates is simply a cylindrical system of coordinates for each of subdomains 1 and 3. Subdomain 1 is always defined in such a way that it contains the logging tool, while subdomain 2 is designed to glue subdomain 1 with subdomain 3 so that the resulting system of coordinates is globally continuous, bijective, and has a positive Jacobian. In the new system of coordinates, material properties are invariant with respect to the quasi-azimuthal direction ζ_2 .

Variational formulation in the new system of coordinates and Fourier series expansion

The change of coordinates defined in equation 3 can be described by the mapping $\mathbf{x} = \psi(\boldsymbol{\zeta})$, which is bijective, with positive Jacobian determinant and globally continuous, as needed for proper finite element computations (see Demkowicz, 2006, Chapter 12). Given any arbitrary scalar-valued function h , we define $\tilde{h} = h \cdot \psi$. Using the chain rule, we obtain

$$\nabla u = \sum_{i,n=1}^3 \frac{\partial \tilde{u}}{\partial \zeta_n} \frac{\partial \zeta_n}{\partial x_i} \mathbf{e}_i = (\mathbf{J}^{-1})^T \frac{\partial \tilde{u}}{\partial \boldsymbol{\zeta}}, \quad (6)$$

where \mathbf{e}_i is the unit vector in the x_i -direction, $\partial \tilde{u} / \partial \boldsymbol{\zeta}$ is a vector with the n th component being $\partial \tilde{u} / \partial \zeta_n$, superscript T denotes transposition, and the Jacobian matrix \mathbf{J} (that is associated with the change of coordinates) is given by

$$\mathbf{J} = \left\{ \frac{\partial x_i}{\partial \zeta_j} \right\}_{i,j=1,2,3} = \begin{pmatrix} f_1' + \cos \zeta_2 & -\zeta_1 \sin \zeta_2 & 0 \\ \sin \zeta_2 & \zeta_1 \cos \zeta_2 & 0 \\ 0 & 0 & 1 \end{pmatrix}. \quad (7)$$

Equation 5 can be expressed in the new system of coordinates $\boldsymbol{\zeta}$, as

$$\begin{cases} \text{Find } \tilde{u} \in \tilde{H}_D^1(\tilde{\Omega}) \text{ such that :} \\ \left\langle \frac{\partial \tilde{v}}{\partial \boldsymbol{\zeta}}, \tilde{\sigma}_{NEW} \frac{\partial \tilde{u}}{\partial \boldsymbol{\zeta}} \right\rangle_{L^2(\tilde{\Omega})} = \langle \tilde{v}, \tilde{f}_{NEW} \rangle_{L^2(\tilde{\Omega})} + \langle \tilde{v}, \tilde{g}_{NEW} \rangle_{L^2(\tilde{\Gamma}_N)} \\ \forall \tilde{v} \in \tilde{H}_D^1(\tilde{\Omega}), \end{cases}$$

where $\tilde{\Omega} = \Omega \circ \psi$, and $\langle \cdot, \cdot \rangle_{L^2(\tilde{\Omega})}$ is the L^2 -inner product of two arbitrary (possibly complex-valued) functions h_1 and h_2 , which is defined as

$$\langle h_1, h_2 \rangle_{L^2(\tilde{\Omega})} = \int_{\tilde{\Omega}} h_1^* h_2 d\zeta_1 d\zeta_2 d\zeta_3, \quad (9)$$

(where $*$ means a complex conjugate)

and

$$\tilde{H}_D^1(\tilde{\Omega}) = \left\{ \tilde{u} \in L^2(\tilde{\Omega}) : \tilde{u}|_{\tilde{\Gamma}_D} = 0, \mathbf{J}^{-1T} \frac{\partial \tilde{u}}{\partial \boldsymbol{\zeta}} \in L^2(\tilde{\Omega}) \right\},$$

$$\tilde{\sigma}_{NEW} := \mathbf{J}^{-1} \tilde{\sigma} \mathbf{J}^{-1T} |\mathbf{J}|,$$

$$\tilde{f}_{NEW} := \tilde{f}|\mathbf{J}|, \quad (f = \nabla \cdot \mathbf{j}^{\text{imp}}), \quad \text{and}$$

$$\tilde{g}_{NEW} := \tilde{g}|\mathbf{J}_S|,$$

where $|\mathbf{J}|$ is the determinant of the Jacobian matrix associated with the above change of variables, and $|\mathbf{J}_S|$ is the determinant of the Jacobian matrix corresponding to Γ_N . (In the remainder of the paper, the symbol ‘ \sim ’ will be omitted for convenience.)

Any function w in the new system of coordinates is periodic (with a period equal to 2π) with respect to ζ_2 , and thus can be expressed in terms of its Fourier series expansion as

$$w = \sum_{l=-\infty}^{l=\infty} w_l e^{jl\zeta_2} = \sum_{l=-\infty}^{l=\infty} F_l(w) e^{jl\zeta_2}, \quad (10)$$

where $e^{jl\zeta_2}$ is the l th mode, and $w_l = F_l(w) = 1/2\pi \int_0^{2\pi} w e^{-jl\zeta_2} d\zeta_2$ is the l th modal coefficient that is independent of ζ_2 .

Using the Fourier series expansion representation for u , σ_{NEW} , f_{NEW} and g_{NEW} , selecting a mono-modal test function $v = v_k e^{jk\zeta_2}$ (where the Fourier modal coefficient v_k is a function of ζ_1 and ζ_3), and considering orthogonality of the Fourier modes in $L^2([0, 2\pi])$, the variational problem (equation 8) can be reduced by linearity to (Pardo et al., 2008).

$$\left\{ \begin{array}{l} \text{Find } u = \sum_l F_l(u) e^{jl\zeta_2} \in H_D^1(\Omega) \text{ such that:} \\ \sum_{l=-\infty}^{l=\infty} \left\langle F_k \left(\frac{\partial v}{\partial \zeta} \right), F_{k-l}(\sigma_{NEW}) F_l \left(\frac{\partial u}{\partial \zeta} \right) \right\rangle_{L^2(\Omega_{2D})} \\ = \langle F_k(v), F_k(f_{NEW}) \rangle_{L^2(\Omega_{2D})} \\ + \langle F_k(v), F_k(g_{NEW}) \rangle_{L^2(\Gamma_N(\Omega_{2D}))} \forall F_k(v) e^{jk\zeta_2} \in H_D^1(\Omega), \end{array} \right. \quad (11)$$

where $\Omega_{2D} = \{(\zeta_1, \zeta_2, \zeta_3) \in \Omega: \zeta_2 = 0\}$, and

$$F_k \left(\frac{\partial v}{\partial \zeta} \right) = \frac{\partial (F_k(v) e^{jk\zeta_2})}{\partial \zeta} e^{-jk\zeta_2} \quad \text{and} \quad (12)$$

$$F_l \left(\frac{\partial u}{\partial \zeta} \right) = \frac{\partial (F_l(u) e^{jl\zeta_2})}{\partial \zeta} e^{-jl\zeta_2}.$$

Considering a bilinear form $b(\alpha_1, \alpha_2)$ and a linear form $l(\alpha_3)$ (which are linear in both variables α_1 and α_2 , and linear in a variable α_3 , respectively), we can define

$$b_l^k F_l(u) = b(F_l(u), F_k(v))$$

$$= \left\langle F_k \left(\frac{\partial v}{\partial \zeta} \right), F_{k-l}(\sigma_{NEW}) F_l \left(\frac{\partial u}{\partial \zeta} \right) \right\rangle_{L^2(\Omega_{2D})}, \quad (13)$$

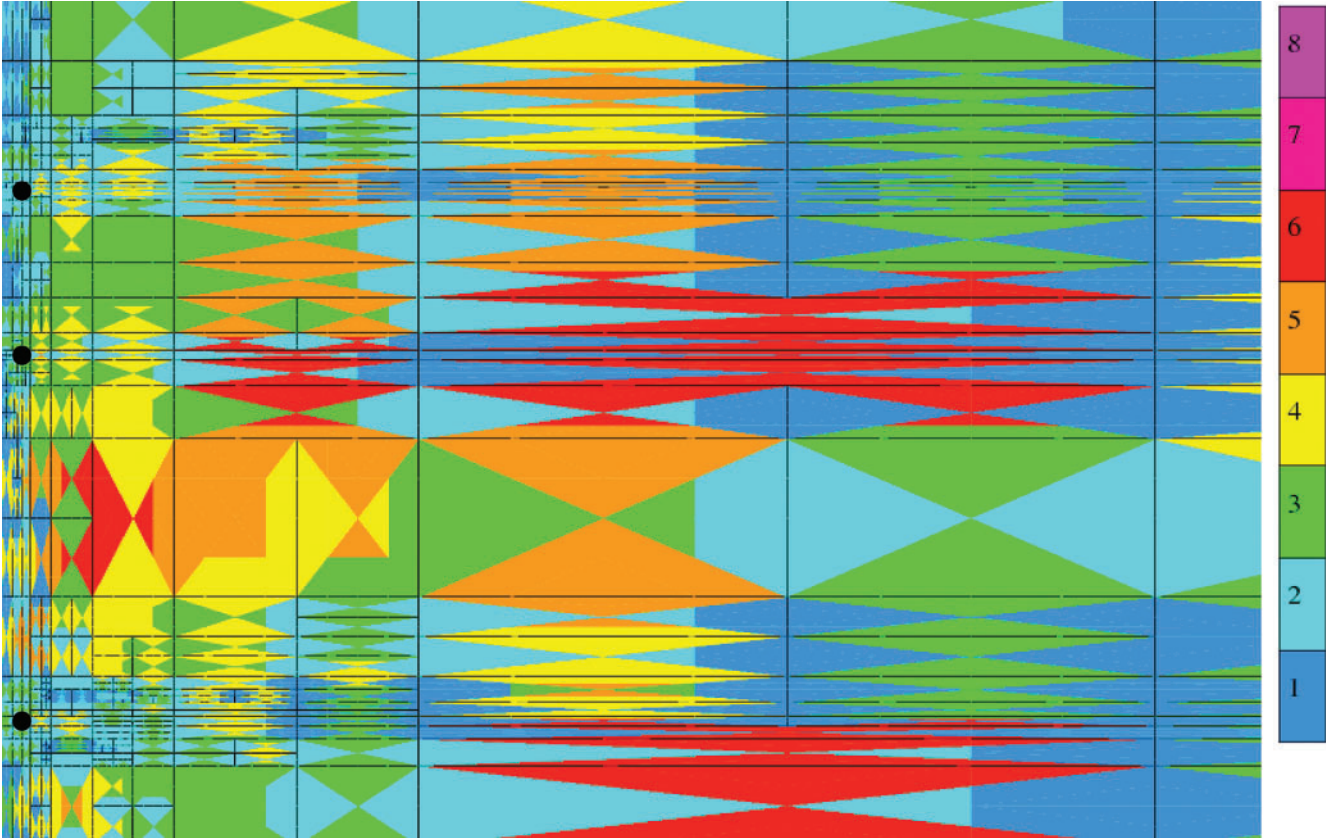


Fig. 3. Two-dimensional self-adaptive goal-oriented hp -grid corresponding to a resistivity logging simulation in a borehole environment. The simulation includes one transmitter (lower solid circle) and two receiver antennas (upper two solid circles). Different colours correspond to different polynomial orders of approximation, from 1 (dark blue) up to 8 (pink).

and

$$l^k = l(F_k(v)) = \langle F_k(v), F_k(f_{NEW}) \rangle_{L^2(\Omega_{2D})} + \langle F_k(v), F_k(g_{NEW}) \rangle_{L^2(\Gamma_N(\Omega_{2D}))}. \quad (14)$$

Using the above definitions, we can express formula 11 in matrix form for the case of, for example, seven Fourier modes ($-3 \leq k \leq 3$) as

$$\begin{bmatrix} b_{-3}^{-3} & b_{-2}^{-3} & b_{-1}^{-3} & b_0^{-3} & b_1^{-3} & b_2^{-3} & b_3^{-3} \\ b_{-3}^{-2} & b_{-2}^{-2} & b_{-1}^{-2} & b_0^{-2} & b_1^{-2} & b_2^{-2} & b_3^{-2} \\ b_{-3}^{-1} & b_{-2}^{-1} & b_{-1}^{-1} & b_0^{-1} & b_1^{-1} & b_2^{-1} & b_3^{-1} \\ b_{-3}^0 & b_{-2}^0 & b_{-1}^0 & b_0^0 & b_1^0 & b_2^0 & b_3^0 \\ b_{-3}^1 & b_{-2}^1 & b_{-1}^1 & b_0^1 & b_1^1 & b_2^1 & b_3^1 \\ b_{-3}^2 & b_{-2}^2 & b_{-1}^2 & b_0^2 & b_1^2 & b_2^2 & b_3^2 \\ b_{-3}^3 & b_{-2}^3 & b_{-1}^3 & b_0^3 & b_1^3 & b_2^3 & b_3^3 \end{bmatrix} \begin{bmatrix} F_{-3}(u) \\ F_{-2}(u) \\ F_{-1}(u) \\ F_0(u) \\ F_1(u) \\ F_2(u) \\ F_3(u) \end{bmatrix} = \begin{bmatrix} l^{-3} \\ l^{-2} \\ l^{-1} \\ l^0 \\ l^1 \\ l^2 \\ l^3 \end{bmatrix} \quad (15)$$

Each component in the above matrix represents a 2D problem in terms of variables ζ_1 and ζ_3 . For subdomains 1 and 3, we have $F_{k-l}(\sigma_{NEW}) = 0$ if $k-l \neq 0$, and thus the above stiffness matrix becomes simply diagonal. Interaction among different 2D problems only occurs in subdomain 2. The fact that the above stiffness matrix in subdomains 1 and 3 becomes diagonal is a major advantage of this formulation over traditional 3D formulations.

A self-adaptive goal-oriented hp -FEM

We employed a 2D self-adaptive goal-oriented high order hp -FEM algorithm (Pardo et al., 2006b), where h indicates the element size and p the polynomial order of approximation, to solve the final 3D variational formulation (equation 11). The self-adaptive hp -refinement strategy automatically conducts an iterative process of optimal (and local) mesh refinements in both h and p . For an element being determined to be refined, the algorithm selects an optimal hp -refinement for the element (Demkowicz, 2006).

The self-adaptive goal-oriented hp -FEM algorithm provides high-accuracy simulations since it converges exponentially fast in terms of the error in the quantity of interest (solution at the receiver electrode) versus the problem size (number of unknowns). Note that the goal-oriented refinement strategy makes optimal hp mesh refinements based on minimizing the error of a prescribed quantity of interest mathematically expressed in terms of a linear functional (Paraschivoiu and Patera, 1998; Oden and Prudhomme, 2001; Prudhomme and Oden, 1999; Heuveline and Rannacher, 2003). To deal with the error in the quantity of interest when generating an optimal grid is critical in the simulation of resistivity-logging measurements, since the solution (electrical potential in this study) at the receiver electrode is typically several orders of magnitude smaller than that around the current electrodes, and thus, a reasonably small (global) absolute error does not imply a small relative error at the receiver.

For a further understanding of optimal hp -grids, Figure 3 shows an example of 2D self-adaptive goal-oriented hp -grid corresponding to a resistivity logging simulation in a borehole environment. We observe heavier refinements (in both h and p) around the transmitter and the two receiver antennas, as physically expected. The outstanding performance of the self-adaptive goal-oriented hp -FEM

algorithm in simulating resistivity-logging measurements has been reported in several papers (e.g. Pardo et al., 2006a, 2006b, 2007; Nam et al., 2009).

Numerical results

When plotting normal logs, we use the middle point between the current electrode and a potential electrode as the reference depth of the logging result. Thus, when the current electrode is at a fixed depth, the logging depth of the long-normal logging is 40 inches above that of short-normal. Simulated potential is transformed into apparent resistivity, ρ_a , using the following formula:

$$\rho_a = \frac{4\pi u}{I} \times l_{AB}, \quad (16)$$

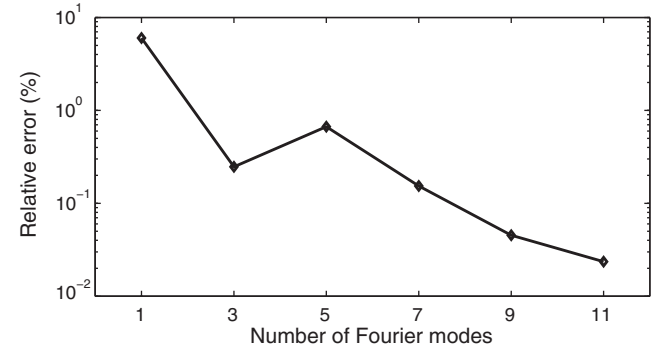


Fig. 4. Convergence behaviour as a function of the number of Fourier modes used in the simulation of short-normal logging measurements in a vertical well penetrating a homogeneous formation whose resistivity is the same as that of borehole, which is equal to $10 \Omega.m$. The diameter of the borehole is equal to 0.4 m.

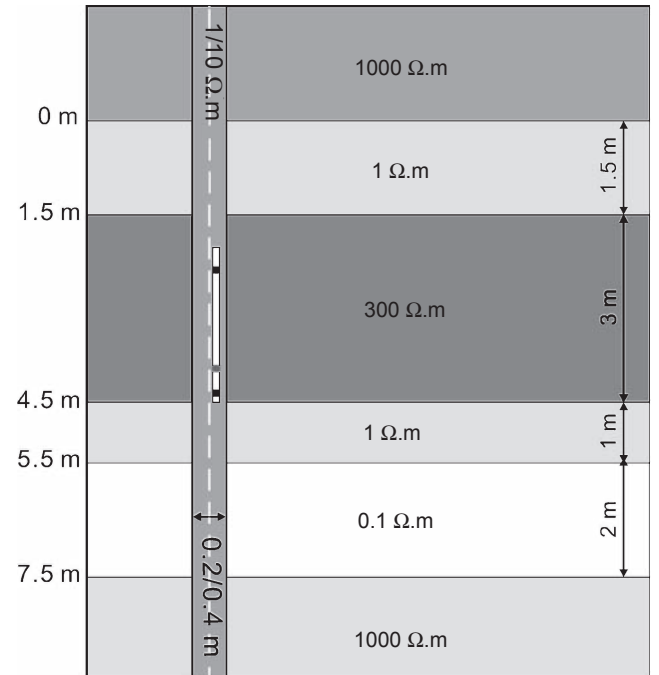


Fig. 5. Formation including six horizontal layers of resistivities equal to 1000, 1, 300, 1, 0.1 and $1000 \Omega.m$ from top to bottom, and a vertical borehole. The thicknesses of the second, third, fourth and fifth layers are 1.5, 3, 1, and 2 m. The borehole has a diameter equal to either 0.2 or 0.4 m, and a resistivity equal to either 1 or $10 \Omega.m$.

where u is the potential at a potential electrode, I is the intensity of the survey current, which is equal to 1 A/m in our simulations, and l_{AB} is the distance between transmitter

and receiver electrodes, which is equal to 64 inches and 16 inches for long- and short-normal measurements, respectively.

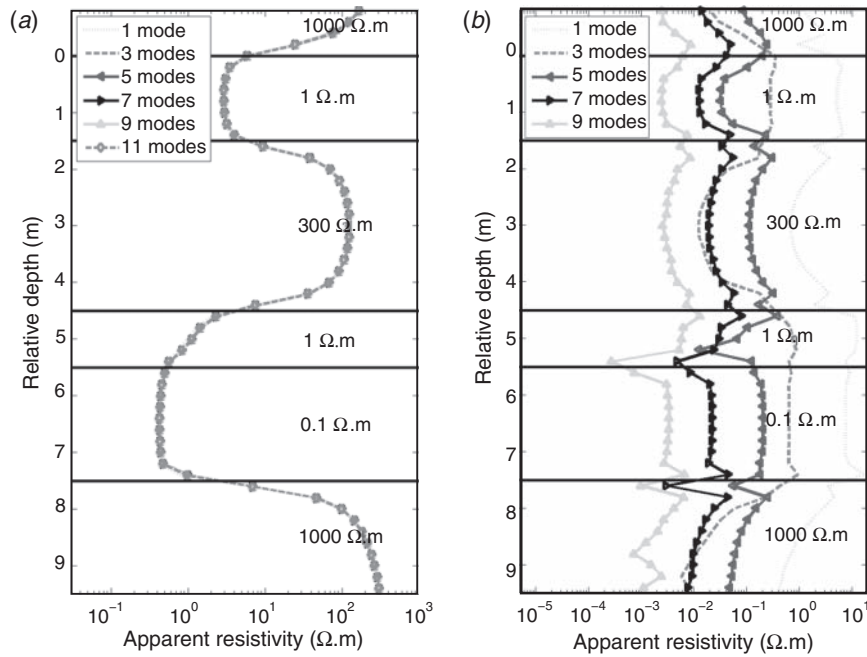


Fig. 6. Short-normal logging measurements in the presence of tool eccentricity of 11.2 cm (panel *a*) for a six-layered formation model (Figure 5) using various numbers of Fourier modes. The borehole with a diameter equal to 0.4 m and a mud resistivity of 10 $\Omega\cdot\text{m}$ penetrates vertically the six-layered formation (1000, 1, 300, 1, 0.1, and 1000 $\Omega\cdot\text{m}$ from top to bottom). The thicknesses of the second, third, fourth, and fifth layers (from top to bottom) are 1.5, 3, 1, and 2 m, respectively. For the computation of relative differences (panel *b*), short-normal logging measurements computed with 11 Fourier modes are regarded as the fully convergent solution and compared with those computed with 1, 3, 5, 7 and 9 Fourier modes.

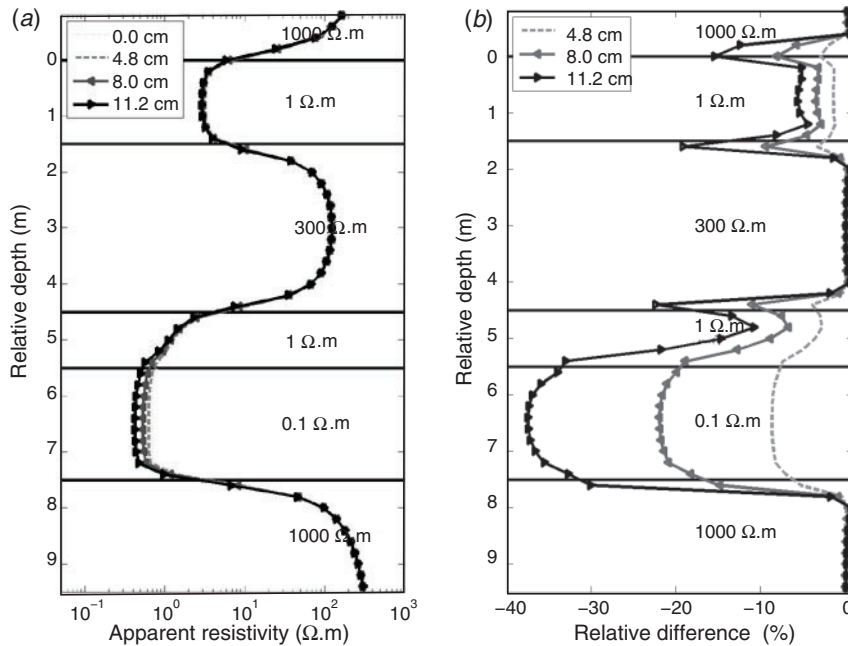


Fig. 7. (a) Short-normal logging measurements in the presence of tool eccentricity in a borehole with a diameter equal to 0.4 m and a mud resistivity of 10 $\Omega\cdot\text{m}$ penetrating a six-layered formation (1000, 1, 300, 1, 0.1, and 1000 $\Omega\cdot\text{m}$ from top to bottom). The thicknesses of the second, third, fourth, and fifth layers (from top to bottom) are 1.5, 3, 1, and 2 m, respectively. (b) Relative differences in percent of the measurements with respect to measurements without tool eccentricity.

Verification of the 3D hp algorithm

To verify the accuracy and reliability of the 3D *hp* algorithm, we consider a borehole 0.4 m in diameter and 10 $\Omega\cdot\text{m}$ in resistivity, and a homogeneous formation whose resistivity is

the same as that of the borehole. The model is thus a homogeneous medium except for the tool properties, and therefore normal logging measurements should coincide with each other regardless of the distances from the centre of the tool to the

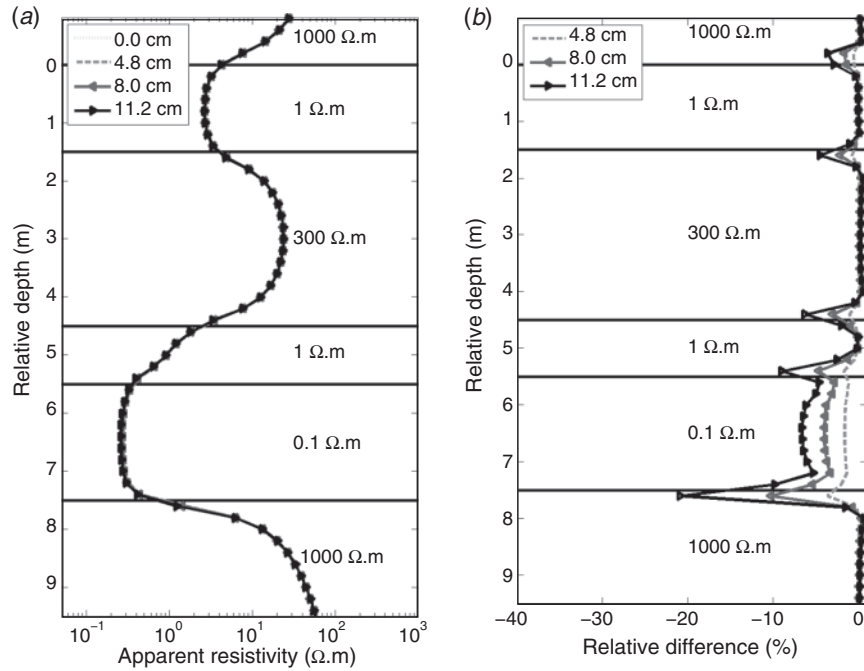


Fig. 8. (a) Short-normal logging measurements in the presence of tool eccentricity in a borehole with diameter equal to 0.4 m and a mud resistivity of 1 $\Omega\cdot\text{m}$ penetrating a six-layered formation (1000, 1, 300, 1, 0.1, and 1000 $\Omega\cdot\text{m}$ from top to bottom). The thicknesses of the second, third, fourth, and fifth layers (from top to bottom) are 1.5, 3, 1, and 2 m, respectively. (b) Relative differences in percent of the measurements with respect to measurements without tool eccentricity.

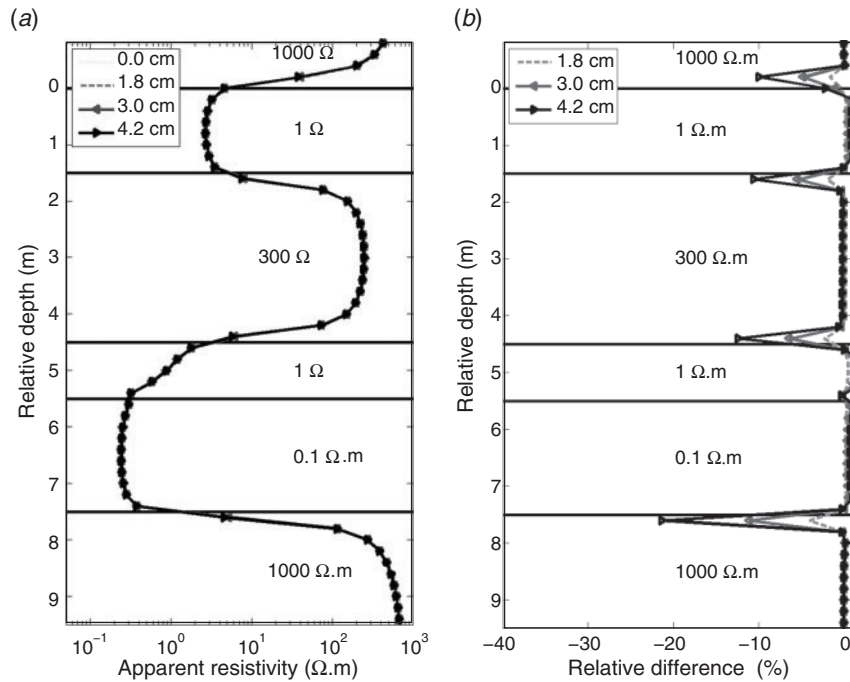


Fig. 9. (a) Short-normal logging measurements in the presence of tool eccentricity in a borehole with diameter equal to 0.2 m and a mud resistivity of 10 $\Omega\cdot\text{m}$, penetrating a six-layered formation (1000, 1, 300, 1, 0.1, and 1000 $\Omega\cdot\text{m}$ from top to bottom). The thicknesses of the second, third, fourth, and fifth layers (from top to bottom) are 1.5, 3, 1, and 2 m, respectively. (b) Relative differences in percent of the measurements with respect to measurements without tool eccentricity.

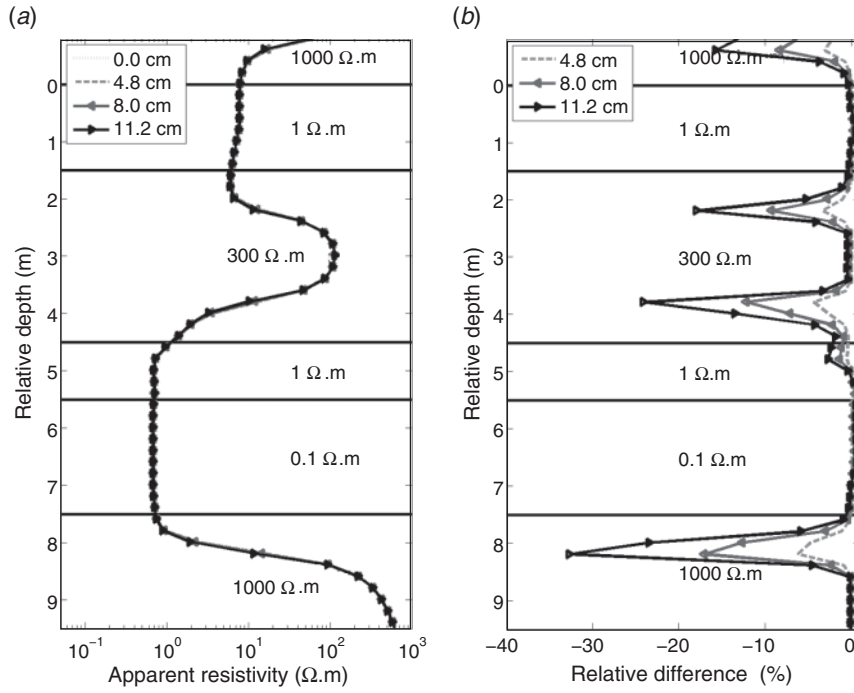


Fig. 10. (a) Long-normal logging measurements in the presence of tool eccentricity in a borehole with diameter equal to 0.4 m and a mud resistivity of 10 Ω .m, penetrating a six-layered formation (1000, 1, 300, 1, 0.1, and 1000 Ω .m from top to bottom). The thicknesses of the second, third, fourth, and fifth layers (from top to bottom) are 1.5, 3, 1, and 2 m, respectively. (b) Relative differences in percent of the measurements with respect to measurements without tool eccentricity.

centre of the borehole axis. Thus, the electric potential in the direction of ζ_2 is constant in subdomain 1, while it varies in subdomains 2 and 3, because the tool is assumed to be eccentric.

Figure 4 displays the relative differences between short-normal logging measurements with tool eccentricity equal to 0.112 m and those obtained with the centralised tool, as we increase the number of Fourier modes. When the tool is centralised, the corresponding problem reduces to 2D, and thus we can do the simulation with our 2D algorithm. For the 2D simulation, we used a 2D *hp*-FEM algorithm which has already been verified in Pardo et al. (2006b). Our 3D formulation, with one Fourier mode, exhibits an error of $\sim 8\%$, which reduces to a level below 1% when more than three Fourier modes are used. We obtain a convergent solution even when using a small number of Fourier modes due to the fact that the solution is smooth along ζ_2 , which was properly selected with that specific objective in mind.

Eccentricity effects on logging measurements

For the analysis on eccentricity effects on normal logging measurements, we consider a formation with six layers whose resistivities are 1000, 1, 300, 1, 0.1, and 1000 Ω .m from top to bottom (Figure 5). The thicknesses of the second, third, fourth, and fifth layers (from top to bottom) are 1.5, 3, 1, and 2 m, respectively. The relative depth of the interface between the first and second layers is set to be zero. The formation has a vertical borehole, which has a resistivity of either 1 or 10 Ω .m, and a diameter of either 0.2 or 0.4 m. The logging tool is assumed to be eccentric from the axis of the borehole by 0.048, 0.08, or 0.112 m in a borehole of diameter 0.4 m, or 0.018, 0.03, or 0.042 m in a borehole with a diameter of 0.2 m.

For further verification of the 3D algorithm, we present the history of convergence of short-normal logging measurements

for the six-layered model as a function of the number of Fourier modes (Figure 6). Differences between results using different numbers of Fourier modes are almost unnoticeable on a log scale (Figure 6a). Figure 6b compares relative differences of short-normal logging measurements using one, three, five, seven, and nine Fourier modes, respectively, with respect to short-normal logging measurements using 11 Fourier modes. Even when using one Fourier mode, the relative differences between the measurements are below $\sim 10\%$. Relative differences decrease with increasing numbers of Fourier modes to a level of $10^{-2}\%$ when using nine Fourier modes.

Eccentricity effects on short-normal measurements in a borehole with a diameter of 0.4 m and a mud resistivity of 10 Ω .m (Figure 7) are largest in the most conductive layer and increase with eccentricity distance specifically in conductive layers; apparent resistivity values in the most conductive layer decrease due to the eccentricity effects. Since more current tends to flow into relatively more conductive layers at the interfaces, the eccentricity effects are large around the interfaces, resulting in a decrease in apparent resistivity as the tool gets closer to the wall of the borehole.

Figure 8 shows eccentricity effects in a conductive 1 Ω .m borehole with a diameter of 0.4 m. Comparison between eccentricity effects in conductive (Figure 8) and resistive boreholes (Figure 7) concludes that a more conductive borehole experiences smaller eccentricity effects than a less conductive one. This is attributed to the fact that less current can penetrate into the formation in conductive boreholes, which means that more current travels inside the conductive borehole.

Eccentricity effects in the interior of the first, third and sixth layers for both 10 Ω .m and 1 Ω .m boreholes (Figures 7b and 8b) are negligible (below 1%), showing minimal increase with eccentricity distance. Furthermore, the increase of eccentricity effects in the 1 Ω .m borehole is also negligible (below 1%) in the

1 Ω .m layer, even though the corresponding eccentricity effects in the 10 Ω .m borehole increase with increasing tool eccentricity (Figure 7b). Thus, we can conclude that tool eccentricity has no serious effects if the borehole is less resistive than formation, because a change in the amount of current flowing into formation is negligible even though the tool gets closer to the wall of borehole; current more willingly flows along the borehole regardless to the eccentricity distance.

Eccentricity effects in a 10 Ω .m borehole with a diameter equal to 0.2 m (Figure 9) are smaller than those in a 10 Ω .m borehole with a diameter equal to 0.4 m (Figure 7). Even though the distance of tool eccentricity is similar, the eccentricity effects are larger in the large borehole (compare eccentricity effects with an eccentricity distance of 0.048 m in Figure 7 with those of 0.042 m in Figure 9).

Figure 10 shows eccentricity effects on long-normal measurements in a borehole with a diameter equal to 0.4 m and a mud resistivity of 1 Ω .m. The eccentricity effects on long-normal measurements are smaller than those on short-normal measurements (compare long-normal measurements (Figure 10) with short-normal measurements (Figure 7)).

Conclusions

We have successfully simulated eccentricity effects on short- and long-normal measurements by combining the use of a Fourier series expansion in a new system of coordinates with a high-order self-adaptive *hp* finite-element method. In the 3D simulation, we modelled a commercial tool that has been used in the Korea Institute of Geoscience and Mineral Resources (KIGAM) for several years. Numerical experiments indicate that our 3D algorithm accurately simulates long- and short-normal logging measurements in the presence of tool eccentricity using only a small number of Fourier modes. Eccentricity effects are larger with increasing distance of tool eccentricity. Resistive logging measurements in a smaller borehole experience smaller eccentricity effects than those in a larger borehole, while eccentricity effects in a more conductive borehole are smaller than in a resistive borehole. Eccentricity effects are more emphasised when the formation is highly conductive.

Acknowledgments

The work reported in this paper was funded by University of Texas at Austin Research Consortium on Formation Evaluation, jointly sponsored by Anadarko, Aramco, Baker Atlas, British Gas, BHPBilliton, BP, Chevron, ConocoPhillips, ENI E&P, ExxonMobil, Halliburton, Hydro, Marathon, Mexican Institute for Petroleum, Occidental Petroleum, Petrobras, Schlumberger, Shell E&P, Statoil, TOTAL, and Weatherford International Ltd, and funded by the Ministry of Land, Transport and Maritime Affairs of Korea. The work of the third author was partially funded by the Spanish Ministry of Science and Innovation under the projects MTM2008-03541, TEC2007-65214, and PTQ08-03-08467.

References

Anon., 1949, Resistivity departure curves, Schlumberger Document No. 3: Schlumberger Well Surveying Corporation.
 Anon., 1969, Resistivity departure curves, Schlumberger Document No. 3: Schlumberger Well Surveying Corporation.
 Demkowicz, L., 2006, Computing with *hp*-adaptive finite elements. Volume I: One and two dimensional elliptic and Maxwell problems: Chapman and Hall.
 Doll, H. G., 1951, The laterolog: A new resistivity logging method with electrodes using an automatic focusing system: *Petroleum Transactions of the AIME*, **192**, 305–316.
 Doll, H. G., 1953, The microlaterolog: *Petroleum Transactions of the AIME*, **198**, 17–31.

Hakvoort, R. G., Fabris, A., Frenkel, M. A., Koelman, J. M. V. A., and Loermans, A. M., 1998, Field measurements and inversion results of the high-definition lateral log: 39th Ann. Log. Symp., Soc. Prof. Log Analysts, paper C.
 Heuveline, V., and Rannacher, R., 2003, Duality-based adaptivity in the *hp*-finite element method: *Journal of Numerical Mathematics*, **11**, 95–113. doi:10.1515/156939503766614126
 Howard, A. Q., and Chew, W. C., 1992, Electromagnetic borehole fields in a layered, dipping-bed environment with invasion: *Geophysics*, **57**, 451–465. doi:10.1190/1.1443259
 Nam, M. J., Pardo, D., and Torres-Verdín, C., 2009, Simulation of DC dual-laterolog measurements in complex formations: A Fourier-series approach with nonorthogonal coordinates and self-adapting finite elements: *Geophysics*, **74**, E31–E43. doi:10.1190/1.3000681
 Oden, J. T., and Prudhomme, S., 2001, Goal-oriented error estimation and adaptivity for the finite element method: *Computers & Mathematics with Applications*, **41**, 735–756. doi:10.1016/S0898-1221(00)00317-5
 Paraschivoiu, M., and Patera, A. T., 1998, A hierarchical duality approach to bounds for the outputs of partial differential equations: *Computer Methods in Applied Mechanics and Engineering*, **158**, 389–407. doi:10.1016/S0045-7825(99)00270-4
 Pardo, D., Demkowicz, L., Torres-Verdín, C., and Paszynski, D., 2006, Simulation of resistivity logging-while-drilling (LWD) measurements using a self-adaptive goal-oriented *hp*-finite element method: *SIAM Journal on Applied Mathematics*, **66**, 2085–2106. doi:10.1137/050631732
 Pardo, D., Demkowicz, L., Torres-Verdín, C., and Tabarovsky, L., 2006, A goal-oriented *hp*-adaptive finite element method with electromagnetic applications. Part I: electrostatics: *International Journal for Numerical Methods in Engineering*, **65**, 1269–1309. doi:10.1002/nme.1488
 Pardo, D., Torres-Verdín, C., and Demkowicz, L., 2007, Feasibility study for two dimensional frequency dependent electromagnetic sensing through casing: *Geophysics*, **72**, F111–F118. doi:10.1190/1.2712058
 Pardo, D., Torres-Verdín, C., Nam, M. J., Paszynski, M., and Calo, V. M., 2008, Fourier series expansion in a non-orthogonal system of coordinates for the simulation of 3D alternating current borehole resistivity measurements: *Computer Methods in Applied Mechanics and Engineering*, **197**, 3836–3849. doi:10.1016/j.cma.2008.03.007
 Pirson, S. J., 1963, Handbook of well log analysis for oil and gas formation evaluation: Prentice Hall Inc.
 Prudhomme, S., and Oden, J. T., 1999, On goal-oriented error estimation for elliptic problems: application to the control of pointwise errors: *Computer Methods in Applied Mechanics and Engineering*, **176**, 313–331. doi:10.1016/S0045-7825(98)00343-0
 Tabarovsky, L. A., Goldman, M. M., Rabinovich, M. B., and Strack, K.-M., 1996, 2.5-D modeling in electromagnetic methods of geophysics: *Journal of Applied Geophysics*, **35**, 261–284. doi:10.1016/0926-9851(96)00025-0
 Tamarchenko, T., and Druskin, V., 1993, Fast modeling of induction and resistivity logging in the model with mixed boundaries: 34th Ann. Log. Symp., Soc. Prof. Well Log Analysts, paper GG.
 Tamarchenko, T., Frenkel, M., and Mezzatesta, A., 1999, Three-dimensional modeling of resistivity devices. In M. Oristaglio, and B. Spies, (Eds), Three-dimensional electromagnetic, Soc. Expl. Geophys., 600–610.
 Tsang, L., Chan, A., and Gianzero, S., 1984, Solution of the fundamental problem of resistivity logging with a hybrid method: *Geophysics*, **40**, 1596–1604.
 Zhang, L., Poulton, M. M., and Wang, T., 2002, Borehole electrical resistivity modeling using neural networks: *Geophysics*, **67**, 1790–1797. doi:10.1190/1.1527079

Manuscript received 10 September 2009; accepted 9 December 2009.